Appl. Phys. B 68, 863–869 (1999) / DOI 10.1007/s003409900022

Applied Physics B
Lasers
and Optics
© Springer-Verlag 1999

Two-wave-mixing dynamics and nonlinear hot-electron transport in transverse-geometry photorefractive quantum wells studied by moving gratings

S. Balasubramanian[1], I. Lahiri[1], Y. Ding[1], M.R. Melloch[2], D.D. Nolte[1]

[1] Department of Physics, Purdue University, West Lafayette, IN 47907-1396, USA
(Fax: +1-765/494-0706, E-mail: nolte@physics.purdue.edu)
[2] School of Electrical and Computer Engineering, Purdue University, West Lafayette, IN 47907-1285, USA

Received: 26 November 1998/Revised version: 22 January 1999/Published online: 12 April 1999

Abstract. The photorefractive response to an applied electric field is measured in a photorefractive quantum well, providing evidence in favor of the nonlinear transport in the device due to the hot electrons. The reduced mobility of the hot electrons limits the drift length, and thereby limits fringe overshoot. Thus the nonlinear transport prevents the slowing down of the grating writing rate for increasing fields which is common in bulk photorefractives. The photorefractive phase shift in transverse-field photorefractive quantum wells is measured as a function of the frequency offset between two laser writing beams that generate moving gratings. The two-wave mixing passes through a maximum at an optimum frequency which depends on the magnitude and the sign of the applied dc electric field. The phase shift associated with the moving grating adds or subtracts from the static phase shift induced by hot-electron transport in the semiconductor quantum wells, depending on the sign of the field and the sign of the dominant photocarriers. We observe a linear relationship between the roll-off frequency and the power of the writing beams.

PACS: 42.40; 42.65; 78.65

Photorefractive quantum wells operating in the transverse-field geometry exhibit a photorefractive phase shift under an applied dc electric field that could not be attributed to trap limitation [1]. The presence of the phase shift led to nonreciprocal energy transfer during two-wave mixing, and produced record photorefractive gains in excess of 1000 cm^{-1} in these devices [2]. The nonlocal dielectric response produced a “turn-on” voltage signature that was reminiscent of the Gunn-effect mechanism in doped GaAs [3], which led to the suggestion that the photorefractive phase shift in the quantum wells was a consequence of nonlinear transport and electron velocity saturation [4]. This hypothesis was verified experimentally in 1996 when a direct experimental connection was made between the phase shift and the structure of the conduction band valleys [5]. Clear evidence for the simultaneous onset of transport nonlinearity due to electron heating and the onset of the photorefractive phase shift were seen in experiments performed on several different samples whose band structures had been specifically engineered.

The nonlocal dielectric response associated with the electron heating and nonlinear transport has important consequences for applications such as laser-based ultrasound detection. Two-wave mixing in photorefractive quantum wells has been used to perform homodyne detection of surface displacements [6]. In these experiments, the relative phase between the signal wave and the local oscillator must be equal to 90°. This phase relationship is needed to achieve maximum linear detection of surface displacements. Because the photorefractive quantum well acts as an adaptive beam combiner, the photorefractive phase shift contributes to the relative phase of the signal and local oscillator, and therefore is of practical interest for this application.

In this paper, we perform a detailed study of the two-wave-mixing dynamics in transverse-field photorefractive quantum wells using running gratings, paying special attention to the role played by the hot-electron photorefractive phase shift. The moving gratings produce an additional shift of the space-charge grating relative to the intensity pattern. This shift can add constructively or destructively with the static hot-electron phase shift, producing changes in the sign for some grating velocities. The principal aspects of the hot-electron phase shift are discussed in Sect. 1, and the device design, fabrication, and characterization are discussed in Sect. 2. The experiments are described in Sect. 3, which has two parts: one that addresses the hot-electron effect on the grating response time in the absence of moving gratings; and one that includes the effects of running gratings. One of the interesting aspects of the hot-electron transport nonlinearity in photorefractive quantum wells is the absence of field-induced slowing down of the grating response time in

---

Dedicated to Prof. Dr. Eckard Krätzig on the occasion of his 60th birthday.

spite of the large fields that are applied. This has the important consequence that the photorefractive quantum wells can maintain high speeds despite the use of high fields. This feature is unique to the photorefractive quantum wells and to the nonlinear transport effects of the hot electrons.

1 Hot electrons

In AlGaAs/GaAs multiple quantum wells, the quasi-equilibrium transport regime can be characterized by the change in the electron mobility as electrons are transferred from the direct conduction-band minima to the higher energy conduction-band valleys. The electric field heats the carriers, raising their energy which produces inter-valley scattering events to scatter them to the indirect valleys. These hot electrons have a strong nonlinear velocity vs. field behavior. The transport of hot holes on the other hand, is linear in applied electric field [7]. Electron-transport nonlinearities may arise from several different mechanisms, including inter-valley transfer, real-space transfer, and field-enhanced deep-level-defect capture-cross-sections [8, 9]. Photorefractive instabilities may be a direct consequence of nonlinear electron transport [10] .

Under large electric fields the electron temperature, T_e, can be significantly larger than the lattice temperature, T_L. The electron temperature and the drift velocity $v(E)$, are related to the energy-relaxation time τ_r, by the quasi-equilibrium approximation [11] as

$$eEv(E) = \frac{3}{2}k_\mathrm{B}\left(\frac{T_\mathrm{e}-T_\mathrm{L}}{\tau_\mathrm{r}}\right) . \tag{1}$$

It follows that the electron temperature is

$$T_\mathrm{e} = T_\mathrm{L} + \frac{2e\tau_\mathrm{r}v(E)}{3k_\mathrm{B}}E . \tag{2}$$

In a two-valley model the electric-field-dependent average mobility is given by

$$\mu(E) = f(E)\mu_\mathrm{l} + [1 - f(E)]\,\mu_\mathrm{u} , \tag{3}$$

where $f(E)$ is the fraction of electrons in the lower energy valley, and μ_l and μ_u are the mobilities of the electrons in the lower and the upper valleys, respectively. To model the photorefractive response we considered a phenomenological hot-electron transport model. The electron fraction in the lower valley is given by [3]

$$f(E) = \left[1 + R\exp\left(-\Delta U/k_\mathrm{B}T_\mathrm{e}\right)\right]^{-1} , \tag{4}$$

where T_e is the electron temperature, which is a function of the applied electric field E, k_B is the Boltzmann constant, and R is the density-of-states ratio between the upper and the lower valleys. For GaAs, R takes a value of 96, ΔU is 0.3 eV, and the electron velocity is

$$v(E) = \frac{\left[\mu_\mathrm{l} + \mu_\mathrm{u}R\exp\left(-\Delta U/k_\mathrm{B}T_\mathrm{e}\right)\right]}{1 + R\exp\left(-\Delta U/k_\mathrm{B}T_\mathrm{e}\right)}E . \tag{5}$$

For electric fields of 4 kV/cm, the electron temperature is higher than the lattice temperature by several hundred degrees. This temperature is sufficient to promote the hot electrons into the indirect conduction band minima that are present in semiconductors such as GaAs and InP. Electrons in these minima have significantly lower mobilities, leading to a strongly nonlinear velocity vs. field dependence. When the velocity saturates, the differential mobility $\mathrm{d}v/\mathrm{d}E$ vanishes [4]. This implies that the electron dielectric relaxation almost vanishes and charge is unable to relax. This drives the space-charge into saturation and leads to a $\pi/2$ photorefractive phase shift.

2 Sample design, fabrication and characterization

The samples used in our experiments were photorefractive multiple quantum wells grown by molecular beam epitaxy (MBE). The structures were MBE $\mathrm{Al_{0.3}Ga_{0.7}As/GaAs}$ multiple quantum wells (MQW) grown on semi-insulating GaAs substrates. Capping and stop-etch layers were grown on a semi-insulating GaAs substrate at 600 °C, followed by an MQW layer grown at 600 °C consisting of a 100-period superlattice of 70 Å GaAs wells and 60 Å $\mathrm{Al_{0.3}Ga_{0.7}As}$ barriers. The samples were proton implanted at a flux of $2\times10^{12}\ \mathrm{cm^{-2}}$ at 160 keV and then at a flux of $1\times10^{12}\ \mathrm{cm^{-2}}$ at 80 keV to make them semi-insulating with uniform defect densities. The substrate is opaque and is removed for transmission studies. The samples were epoxied onto glass and the substrate was removed using a dilute ammonium hydroxide etch, which stops at the AlGaAs stop-etch layer. The stop-etch layer was then removed using a dilute hydrofluoric acid flash for about 15 s using a 40% dilute solution, and two coplanar gold contacts were evaporated on the top layer.

The samples were characterized using an infrared spectrometer, and the results are shown in Fig. 1. The change in transmission of the sample due to an applied electric field was measured using a silicon photodiode connected to a lock-in amplifier. The differential transmission is shown as a function of wavelength for several applied electric fields in Fig. 1a. This gives the wavelength location of the exciton and the optimum electric field to use for best performance in the mixing experiments, which were performed at an applied field of 0.75 V/μm. The change in absorption is calculated from the differential transmission using the relation

$$\Delta\alpha = -\frac{1}{L}\ln\left(1 + \frac{\Delta T}{T}\right) , \tag{6}$$

where L is the thickness of the active electro-optic layer, and is plotted as a function of wavelength for several applied electric fields in Fig. 1b. The change in refractive index is obtained from the change in absorption using the Kramers–Kronig relations, and is shown in Fig. 1c.

3 Experiments

3.1 Hologram response time – testing the hot-electron model

For the hologram response time study, degenerate four-wave mixing was performed using a CW Ti:sapphire laser tuned to 836 nm. The beam intensity ratio of the two hologram-writing beams was 1 : 1 with the polarization of one beam modulated by 90° using an electro-optic modulator (ConOptics 350-80)

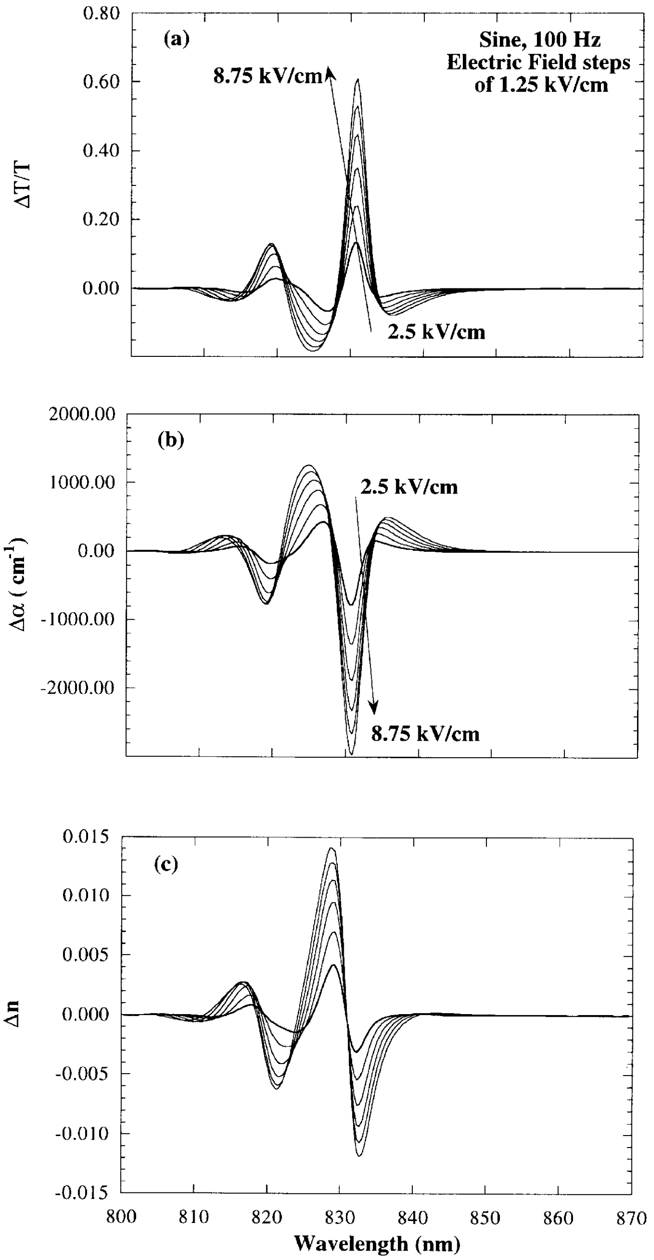

Fig. 1a–c. Differential transmission (**a**), change in absorption (**b**), and the corresponding change in refractive index (**c**) for several applied electric fields. The electric field is a dc field modulated at 100 Hz

with a bandwidth of 200 kHz. The diffracted beam is detected with a high-gain avalanche photodetector (Hamamatsu APD C5460-01) with a response time of approximately 3 μs. The combined system (modulator and detector) had a response time of approximately 4.5 μs.

The photorefractive response time is an important parameter that enables one to verify the validity of the use of the nonlinear hot-electron transport model. The electric field in the photorefractive effect is the spatially modulated space-charge field. Therefore, the time required for this field to build up depends on many factors influencing the charge photoexcitation, transport, and redistribution. Under spatially inhomogenous light illumination, the space-charge field develops until it is balanced by the relaxation due to the conductivity of the material. For a temporal step function of an intensity interference pattern with a spatial sinusoidal structure, the amplitude of the first spatial harmonic of the space-charge field has a simple response function, given by [12, 13]

$$E_{\mathrm{SC}}(t) = mE_{\mathrm{SC}}^{\mathrm{Max}}\left(1 - e^{-t/\tau_{\mathrm{R}}}\right) , \tag{7}$$

with the maximum amplitude $E_{\mathrm{SC}}^{\mathrm{Max}}$ and the intensity modulation depth

$$m = 2\frac{(I_1 I_2)^{1/2}}{(I_1 + I_2)} . \tag{8}$$

In the case of drift-dominated transport (in the absence of hot-electron effects) the field response time τ_{R} is given by [14]

$$\begin{aligned} \tau_{\mathrm{R}} &= \frac{\varepsilon\varepsilon_0}{\sigma_{\mathrm{p}} + \sigma_{\mathrm{d}}}\left[1 + \left(K_{\mathrm{g}} L_E\right)^2\right] \\ &= \frac{\varepsilon\varepsilon_0}{(I\alpha\tau + n_{\mathrm{d}})\, e\mu}\left[1 + \left(K_{\mathrm{g}} L_E\right)^2\right] , \end{aligned} \tag{9}$$

where ε is the dielectric constant, $\sigma_{\mathrm{p,d}}$ are the photo- and dark conductivity, respectively, I is the light intensity with a unit of photon flux density, α is the absorption coefficient, τ is the carrier lifetime, n_{d} is the dark carrier density, μ is the bipolar mobility, $K_{\mathrm{g}} = 2\pi/\Lambda$ is the grating vector with grating spacing Λ, and $L_E = \mu\tau E$ is the photocarrier drift length under an electric field E. For no applied field ($E = 0$), the response time is simply the dielectric relaxation time, which is inversely proportional to the light intensity. At the saturation intensity, which is the intensity needed for the photoconductivity to compensate the dark conductivity ($\approx 100\,\mathrm{nW/cm^2}$ for our samples with a dark resistivity of $10^9\ \Omega\,\mathrm{cm}$), the dielectric relaxation time is about 1 ms. At higher intensities, the dielectric relaxation time decreases.

In four-wave-mixing experiments, it is the temporal behavior of the diffracted signal that is measured instead of the space-charge field itself. The diffracted beam intensity is proportional to the square of the change in the refractive index. For transverse PRQWs based on the Franz–Keldysh effect, the refractive index is approximately proportional to the square of the space-charge field, in the low field regime ($E < 6\,\mathrm{kV/cm}$). Therefore, theoretically, the temporal function of the diffracted signal is given by

$$I_{\mathrm{D}}(t) = I_{\mathrm{D}}^{\mathrm{Max}}\left(1 - e^{-t/\tau_{\mathrm{R}}}\right)^2 . \tag{10}$$

By measuring the temporal buildup of the diffracted signal and fitting with (10), the space-charge-field response time can be deduced. However, due to the sub-quadratic dependence of the refractive index on the field and other factors, (10) is not an exact expression of the time-dependence function of the diffracted signal. For simplicity, we define the response time of the diffracted signal τ_{D} as the time needed to reach $(1 - 1/e)$, i.e. 63% of its steady-state value. From (10) we get the relationship between τ_{D} and τ_{R} as $\tau_{\mathrm{D}} = 1.6\tau_{\mathrm{R}}$ and τ_{D} behaves identically to τ_{R} as far as its dependence on the physical parameters such as electric field and light intensity are concerned.

Figure 2 shows a typical temporal response of the diffracted signal with step-like hologram writing beams at three different light intensities, showing that higher light intensity produces faster response, with possible overshoot at

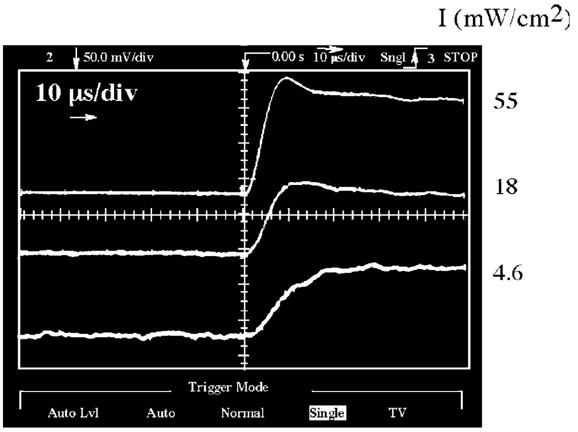

Fig. 2. Photograph showing the typical time response of the diffracted signal from the hologram with step-like writing beams. The three traces correspond to three intensities of 4.6 mW/cm^2 (*lower trace*), 18 mW/cm^2 (*middle trace*), and 55 mW/cm^2 (*upper trace*, near the detection limit)

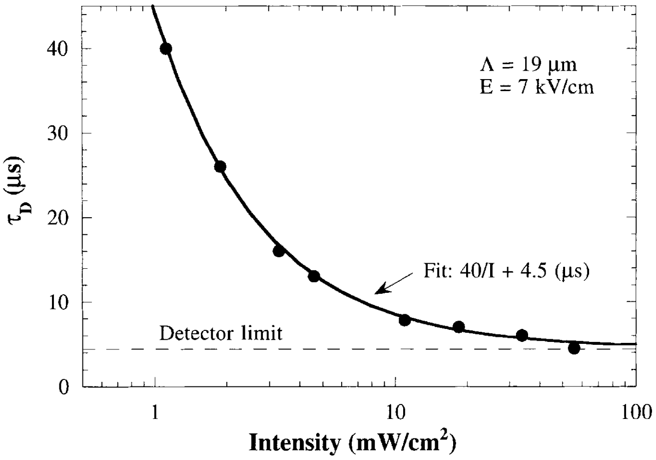

Fig. 3. Measured hologram response time τ_D as a function of incident light intensity. The *curve* in the figure is a fit according to (9) with $\tau_D = 40/I + 4.5\,\mu\text{s}$

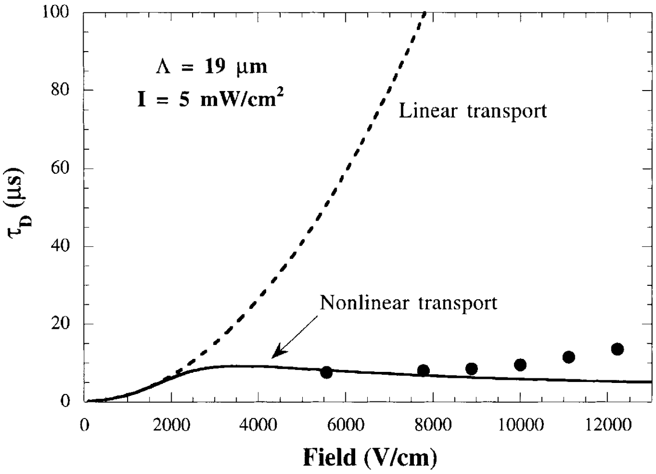

Fig. 4. Hologram response time as a function of applied electric field is plotted as data. The *solid line* is calculated using (9) and the *dotted line* is from the nonlinear transport model including hot electrons [15]

the highest intensities. Figure 3 shows the intensity dependence of the signal response time τ_D measured at 836 nm and at an applied field of 7 kV/cm. The response time asymptotically approaches the detection limit of 4.5 µs at an intensity around 40 mW/cm^2. The curve in the figure is the theoretical $1/I$ fit with a constant detector limit according to (9), with the dark conductivity neglected. The fit agrees well with the experimental data. The intensity used in the figure is the sum of the two writing beam intensities, which are individually obtained by measuring the power and the full-width at half-maximum (FWHM) of the spatial profile of each beam and then corrected from the Fresnel reflection on the semiconductor–air interface. No Fabry–Pérot effects are considered. A convenient benchmark for the PRQW devices is a grating response speed in the range of 250 kHz for an intensity of 10 mW/cm^2. However, this speed depends on the precise proton implant dose for this device, and the speed can be made faster or slower by selective choice of the implant during device fabrication.

The hologram response time would depend on the external applied electric field through the dependence of (9) in the absence of hot-electron effects. Increasing the field would be expected to significantly slow down the response because larger space-charge fields are needed to screen the applied field, which takes longer to build up, and also because photocarriers have large drift lengths at high fields and overshoot the dark fringes, resulting in ineffectiveness in space-charge buildup. However, (9) is not valid in the case of transport nonlinearity, but must be modified by the field-dependence of the electron velocity.

The experimental data of the response time as a function of the applied electric field are shown in Fig. 4 with the theoretical curve using the simple quadratic function in (9), as well as the hot-electron transport calculation in [15]. The experimentally measured response is much faster than the linear-transport curve, providing evidence in favor of the nonlinear transport in the device due to the hot electrons. The reduced mobility of the hot electrons limits the drift length, and thereby limits fringe overshoot. This is a significant side-effect of the hot-electron mechanism that has important consequences for applications. The devices do not slow down under high applied fields, but maintain excellent speed properties.

3.2 Moving gratings

Moving gratings in photorefractive materials have been used to obtain spectroscopic information about the photorefractive recording mechanisms [16], as well as to enhance the photorefractive gain [17]. We use the moving gratings expressly for the former purpose, and are able to extract dynamic information pertaining to the formation of space-charge gratings under hot-electron conditions.

For the moving-grating experiments we performed degenerate two-wave and four-wave mixing using a CW Ti:sapphire laser tuned to 838.5 nm, with a fringe/grating spacing of 21 µm. The experimental setup is as shown in Fig. 5. This setup although similar in design, is different from the one that is used for the hologram response time study that was discussed earlier where the polarization of one beam was modulated by 90° using an electro-optic modulator. Two matched acousto-optic modulators operating at

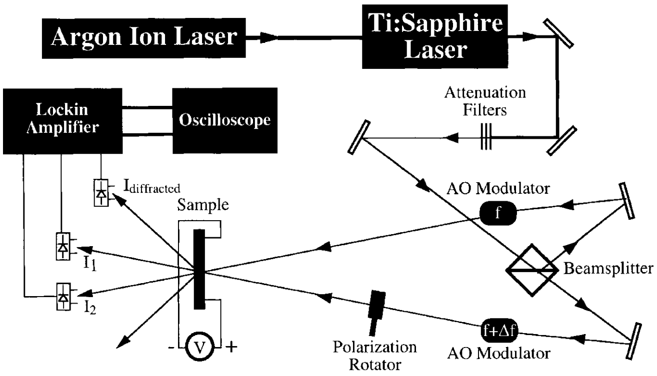

Fig. 5. Experimental setup for two-wave and four-wave mixing with acousto-optic (AO) modulators to introduce a frequency offset between the two mixing beams

center frequencies of 80 MHz controlled the frequency difference between the two writing beams. The running gratings are produced by keeping one of the acousto-optic modulators at a fixed frequency ($f = 80$ MHz) while varying the frequency of the other modulator, $f + \Delta f$. The electric field across the photorefractive quantum well was modulated using a 0.75 V/μm dc field, modulated by a 100 Hz sine wave. The transmitted zero-order beams and the diffracted first-order signals were detected using silicon photodiodes with 650-nm long-pass filters. The transmitted and diffracted signals were recorded as a function of time on a digital storage oscilloscope.

The measured two-wave-mixing gain is given by [15]

$$\gamma_{\mathrm{m}}(E) = 1 + \frac{\beta}{1+\beta}\left[\frac{4\pi n_{\mathrm{m}} L}{\lambda\cos\theta}\sin\phi(E) - \frac{\alpha_{\mathrm{m}} L}{\cos\theta}\cos\phi(E)\right] \tag{11}$$

where β is the ratio of the incident beam intensities and α_{m} and n_{m} are the Fourier components of the absorption and index gratings that would be produced by a maximum modulation. The contribution to the two-wave-mixing gain by the absorption grating is symmetric with respect to the photorefractive phase shift ϕ, whereas the contribution from the index grating is asymmetric.

The two-wave mixing, in arbitrary units, is shown in Fig. 6a as a function of Δf for both positive and negative electric-field directions. There is an optimum frequency detuning at which the two-wave mixing reaches a maximum in the case of positive field, while the gain changes sign at nearly this same frequency for negative fields. The four-wave mixing, in arbitrary units, is shown in Fig. 6b as a function of Δf for both positive and negative electric field and is highly symmetric with respect to the polarity of the electric field. This indicates that the device electrical contacts are symmetric. The photorefractive phase shift is obtained by combining the two-wave-mixing gain measurements with the four-wave-mixing diffraction efficiency η, defined as

$$\sqrt{\eta} = \pi\Delta n L/(\lambda\cos\theta)\ , \tag{12}$$

through

$$\sin\phi = \frac{1}{2\sqrt{\beta}}\frac{\gamma_n}{\sqrt{\eta}}\ , \tag{12a}$$

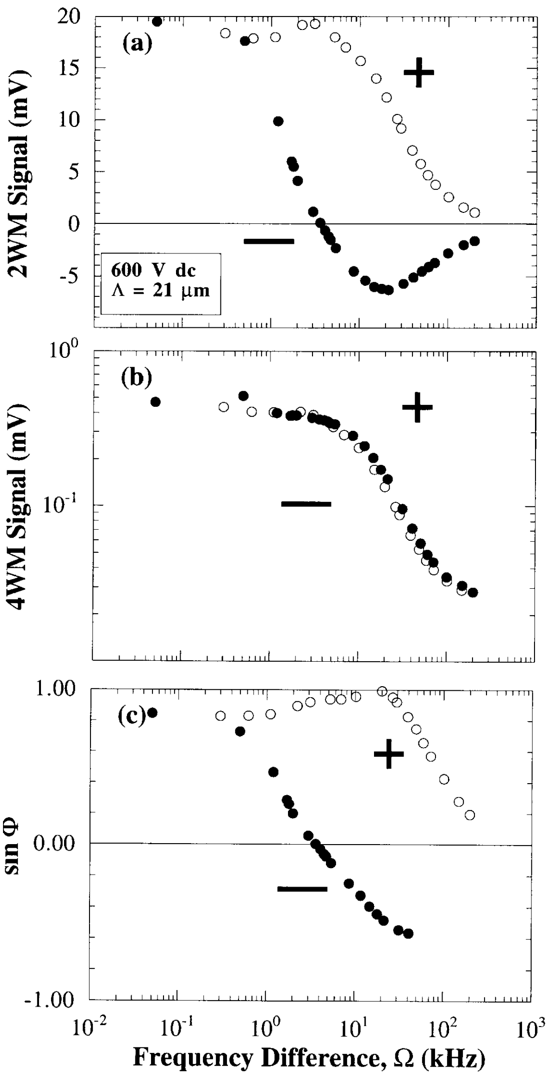

Fig. 6a–c. Two-wave mixing, four-wave mixing, and the sine of the photorefractive phase shift as a function of detuning frequency for an electric field of ±0.75 V/μm. The low-frequency phase shift approaches $\pi/2$ for $E > 0.3$ V/μm due to hot-electron effects associated with the Gunn effect

where

$$\gamma_n = \frac{\gamma(+E) - \gamma(-E)}{2} \tag{13}$$

is defined as only the asymmetric contribution to (11).

The photorefractive phase shift is shown in Fig. 6c as a function of Δf for both field polarities. In the case of positive polarity, the phase shift induced by the lagging gratings adds constructively with the static hot-electron phase shift. At an optimum frequency offset $\Delta f = 20$ kHz, the phase shifts collectively add to $\pi/2$. On the other hand, for negative polarity, the lagging phase shift and the hot-electron phase shift combine destructively and the total phase shift goes through zero around 10 kHz. The total phase shift at low frequency detuning is close to $\pi/2$ for applied fields larger than 3 kV/cm, attributed to the hot-electron effects [4].

The dynamic phase shift that is driven by the lagging space-charge grating is a function of the illumination intensity, which defines the response rate of the space-charge grating formation process. We performed an intensity study

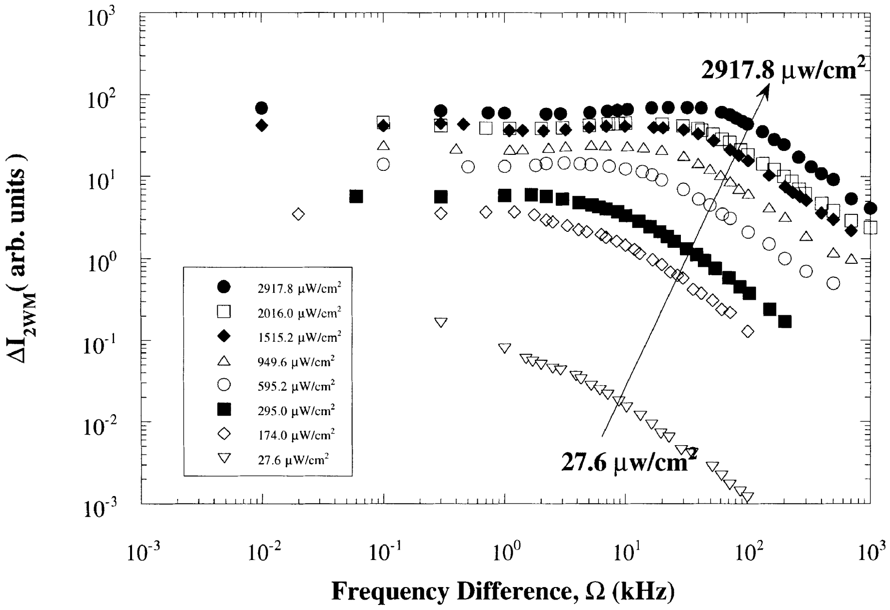

Fig. 7. Two-wave mixing signal, plotted as $\Delta I_{\text{asym}} = \Delta I(+) - \Delta I(-)$, as a function of detuning frequency for increasing beam intensities. The applied field is 0.75 V/μm and the fringe spacing is 21 μm

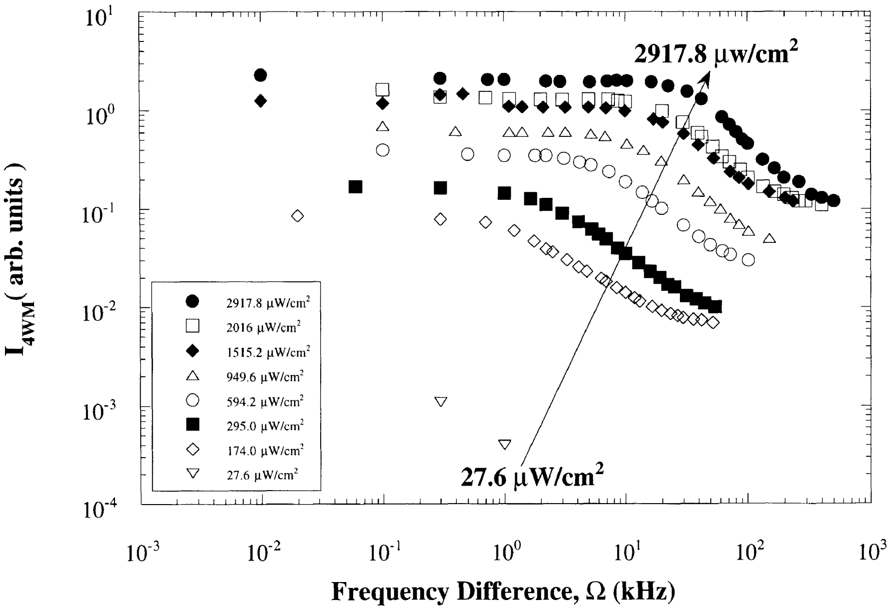

Fig. 8. Four-wave-mixing diffracted intensity plotted as a function of detuning frequency under the same conditions as Fig. 7

of the moving fringes for positive field polarity in which the hot-electron phase shift adds constructively to the lagging phase shift. Figure 7 shows the asymmetric two-wave-mixing data as a function of the frequency difference between the two writing beams for increasing beam intensities. The intensities of the two mixing beams were maintained to be approximately equal in all cases. The photorefractive gain displays a resonant behavior with a peak that coincides with the detuning at which the output diffraction efficiency rapidly decreases, shown in Fig. 8 under the same conditions as in Fig. 7.

The two-wave and four-wave mixing data are combined through (13) to generate $\sin\phi$, which is shown in Fig. 9. The frequency offset that produces a $\pi/2$ phase shift is an increasing function of the total intensity. The frequency at which $\sin\phi = 1$ is plotted in Fig. 10 as a function of laser intensity. The dependence is fit extremely well by a linear function of intensity (up to 3 mW/cm^2 with a roll-off frequency of 70 kHz), which is consistent with the data in Fig. 4, measured under very different conditions. This data also illustrates that the hot-electron effect has the same linear-intensity dependence as for linear transport, despite the significantly different field dependence.

4 Conclusion

We have presented an experimental demonstration of the effect of frequency detuning on the photorefractive phase shift in a transverse-geometry photorefractive MQW using moving gratings. The photorefractive phase shift always achieves a value of $\pi/2$ for positive field polarity at an optimum beam

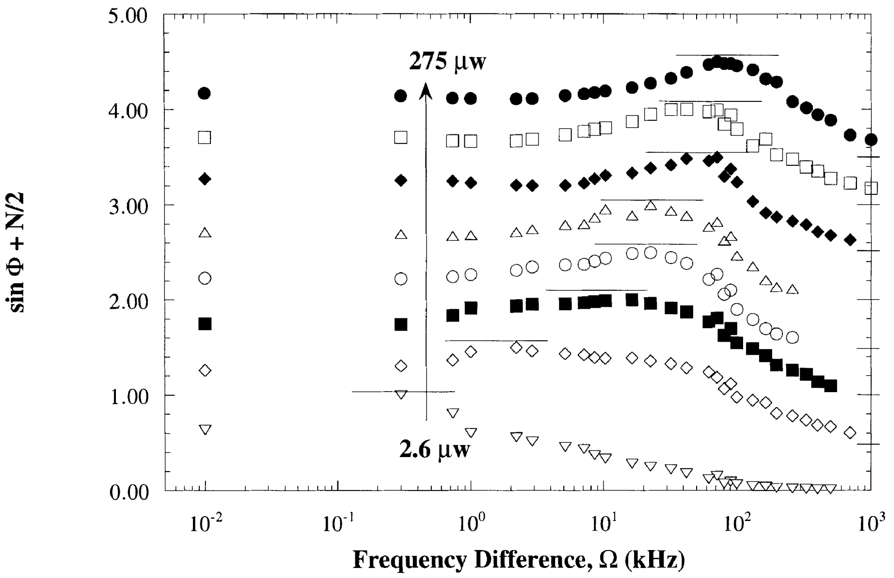

Fig. 9. Sine of the photorefractive phase shift as a function of detuning frequency for different beam intensities under the same conditions as Figs. 7–8. The *curve* for the beam intensity of 2.6 μW is plotted between the correct limits. Successive curves have been offset by $\sin\Phi = 0.5$ from preceding curves. The sine of the photorefractive phase shift has a maximum for every beam intensity at a particular detuning frequency where there is an optimum lag between the moving intensity pattern and the lagging space charge. The *horizontal dashes* on the *y* axis on the *right* denote the zero line for each curve, and the line at the maximum is the $\sin\Phi = 1.0$ line for that curve. The different *symbols* stand for different powers as follows, ● – 275 μW, □ – 190 μW, ♦ – 142.8 μW, △ – 89.5 μW, ○ – 56.0 μW, ■ – 27.8 μW, ◇ – 16.4 μW, ▽ – 2.6 μW

intensity and optimum grating velocity. The cutoff frequency at which the peak photorefractive gain occurs increases linearly with the beam intensities. This linear relationship puts two parameters under our control, the frequency detuning and the mixing beam intensities, that help to tailor the value of the photorefractive phase shift. This may help a number of applications in opto-electronic devices. For instance, demonstrations of optical applications include high-speed image correlators [18], femto-second auto-correlation [19], time-to-space mapping of femto-second pulses [20], as well as adaptive beam combiners for laser-based ultrasound detection [6].

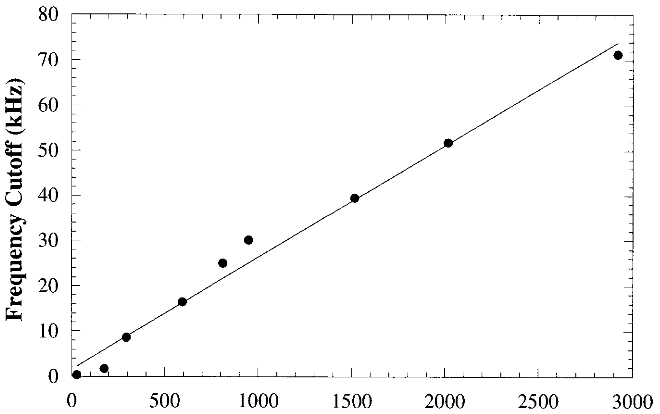

Fig. 10. The detuning frequency cutoff as a function of mixing beam intensity. The applied field is 0.75 V/μm and the fringe spacing is 21 μm

References

1. Q.N. Wang, D.D. Nolte, M.R. Melloch: Appl. Phys. Lett. **59**, 256 (1991)
2. Q.N. Wang, R.M. Brubaker, D.D. Nolte, M.R. Melloch: J. Opt. Soc. Am. B **9**, 1626 (1992)
3. S.M. Sze: *Physics of Semiconductor Devices*, 2nd edn. (Wiley, New York 1981)
4. Q.N. Wang, R.M. Brubaker, D.D. Nolte: J. Opt.Soc. Am. B **11**, 1773 (1994)
5. R.M. Brubaker, Q.N. Wang, D.D. Nolte, M.R. Melloch: Phys. Rev. Lett. **77**, 4249 (1996)
6. I. Lahiri, L.J. Pyrak-Nolte, D.D. Nolte, M.R. Melloch, R.A. Kruger, G.D. Bacher, M.B. Klein: Appl. Phys. Lett. **73**, 1041 (1998)
7. V.L. Dalal: Appl. Phys. Lett. **16**, 489 (1970)
8. B.K. Ridley, P.H. Wisbey: Brit. J. Phys. **18**, 761 (1967)
9. K. Hess, H. Morkoc, H. Schichijo, B.G. Streetman: Appl. Phys. Lett. **55**, 1421 (1989)
10. D.D. Nolte, D.H. Olson, A.M. Glass: J. Appl. Phys. **68**, 4111 (1990)
11. K. Seeger: *Semiconductor Physics*, 5th edn. (Springer, Berlin, Heidelberg 1991)
12. N.V. Kukhtarev: Sov. Tech. Phys. Lett. **2**, 438 (1976)
13. J.P. Huignard, P. Günter: *Photorefractive Materials and Their Applications II* (Springer, Berlin, Heidelberg 1988)
14. D.D. Nolte, D.H. Olson, G.E. Doran, W.H. Knox, A.M. Glass: J. Opt. Soc. Am. B **7**, 2217 (1990)
15. D.D. Nolte, M.R. Melloch: In: *Photorefractive Effects and Materials*, ed. by D.D. Nolte (Kluwer, Dordrecht 1995)
16. G.C. Valley: J. Opt. Soc. Am. B **1**, 868 (1984)
17. B. Imbert, H. Rajbenbach, S. Mallick, J.P. Herriau, J.P. Huignard: Opt. Lett. **13**, 327 (1988)
18. A. Partovi, A.M. Glass, T.H. Chiu, D.T.H. Liu: Opt. Lett. **18**, 906 (1993)
19. R.M. Brubaker, Q.N. Wang, D.D. Nolte, E.S. Harmon, M.R. Melloch: J. Opt. Soc. Am. B **11**, 1038 (1994)
20. M.C. Nuss, M. Li, T.H. Chiu, A.M. Weiner, A. Partovi: Opt. Lett. **19**, 664 (1994)